Army Research Laboratory

Three-Dimensional Bending Analysis of Functionally-Modified Bimorph PZT Actuator for *cm*-Scale Flapping Wing

by Jaret C. Riddick and Asha Hall

ARL-TR-5581 **July 2011**

NOTICES

Disclaimers

Army Research Laboratory

Aberdeen Proving Ground, MD 21005-5069

ARL-TR-5581 **July 2011**

Three-Dimensional Bending Analysis of Functionally-Modified Bimorph PZT Actuator for *cm*-Scale Flapping Wing

Jaret C. Riddick
Vehicle Technology Directorate, ARL

Asha Hall
Motile Robotics, Inc.

REPORT DOCUMENTATION PAGE	*Form Approved OMB No. 0704-0188*

Public reporting burden for this collection of information is estimated to average 1 hour per response, including the time for reviewing instructions, searching existing data sources, gathering and maintaining the data needed, and completing and reviewing the collection information. Send comments regarding this burden estimate or any other aspect of this collection of information, including suggestions for reducing the burden, to Department of Defense, Washington Headquarters Services, Directorate for Information Operations and Reports (0704-0188), 1215 Jefferson Davis Highway, Suite 1204, Arlington, VA 22202-4302. Respondents should be aware that notwithstanding any other provision of law, no person shall be subject to any penalty for failing to comply with a collection of information if it does not display a currently valid OMB control number.

PLEASE DO NOT RETURN YOUR FORM TO THE ABOVE ADDRESS.

1. REPORT DATE *(DD-MM-YYYY)*	2. REPORT TYPE	3. DATES COVERED (From - To)
July 2011	Final	July 2009–March 2011

4. TITLE AND SUBTITLE Three-Dimensional Bending Analysis of Functionally-Modified Bimorph PZT Actuator for *cm*-Scale Flapping Wing	**5a. CONTRACT NUMBER**
	5b. GRANT NUMBER
	5c. PROGRAM ELEMENT NUMBER
6. AUTHOR(S) Jaret C. Riddick and Asha Hall*	**5d. PROJECT NUMBER**
	5e. TASK NUMBER
	5f. WORK UNIT NUMBER
7. PERFORMING ORGANIZATION NAME(S) AND ADDRESS(ES) U.S. Army Research Laboratory ATTN: RDRL-VTM Aberdeen Proving Ground, MD 21005-5069	**8. PERFORMING ORGANIZATION REPORT NUMBER** ARL-TR-5581
9. SPONSORING/MONITORING AGENCY NAME(S) AND ADDRESS(ES)	**10. SPONSOR/MONITOR'S ACRONYM(S)**
	11. SPONSOR/MONITOR'S REPORT NUMBER(S)

12. DISTRIBUTION/AVAILABILITY STATEMENT

Approved for public release; distribution is unlimited.

13. SUPPLEMENTARY NOTES

*Motile Robotics, Inc., Joppa, MD, 21085

14. ABSTRACT

Army combat operations have placed a high premium on reconnaissance missions for micro air vehicles (MAVs). An analysis of insect flight indicates that in addition to the bending excitation (flapping), simultaneous excitation of the twisting degree-of-freedom is required to manipulate the control surface adequately. By adding a layer of angled piezoelectric segments to a $Pb(Zr,Ti)O_3$ (also referred to as PZT) bimorph actuator, a bend-twist coupling may be introduced to the flexural response of the layered PZT, thereby creating a biaxial actuator capable of driving wing oscillation in flapping wing MAVs. The present study presents numerical solutions to governing equations for quasi-static three-dimensional bending of functionally–modified bimorph designs intended for active bend-twist actuation of *cm*-scale flapping wing devices. The results indicate a strong dependence of bimorph deflection on overall length. Further, the width and angle of orientation of the angled piezoelectric segments may be manipulated in order to increase or decrease the length effects on bimorph deflection. The relationships of geometry and orientation of the angled segments with bimorph flexural response are presented.

15. SUBJECT TERMS

piezoelectric, bimorph actuator, three-dimensional bending, functionally-modified, PZT

16. SECURITY CLASSIFICATION OF:			17. LIMITATION OF ABSTRACT	18. NUMBER OF PAGES	19a. NAME OF RESPONSIBLE PERSON
a. REPORT	b. ABSTRACT	c. THIS PAGE			Jaret Riddick
Unclassified	Unclassified	Unclassified	UU	20	19b. TELEPHONE NUMBER *(Include area code)* (410) 278-9831

Standard Form 298 (Rev. 8/98)
Prescribed by ANSI Std. Z3

Contents

List of Figures

List of Tables

1. Introduction

Significant technical strides have been accomplished in designing *cm*-scale micro air vehicles (MAVs). One approach for accomplishing this mission is to develop a biologically inspired flapping wing insect that can maneuver into confined areas and possess hovering capabilities. Insect-like MAVs have great potential for limited duration electronic surveillance and sensor-based detection for both military and civilian missions (*1*). Some advantages of MAVs include portability, low noise, low altitude aerial surveillance, low radar cross section, low power consumption, and ease of generation of lift or thrust at low weight. MAVs are implemented as fixed, rotating, or flapping wing solutions. Fixed wing MAVs use the wing span, the angle of attack as a function of forward airspeed, and the surface area to gain lift and thrust; meanwhile, flapping wing systems generate lift through the flapping wing beat frequency. A significant advantage of the flapping wing systems is lower bandwidth where the cyclic control inputs to maintain lift and stability operate at lower frequencies as compared with a rotor system (*2*). However, due to the size limitations of MAVs (typically, less than 15 cm in dimension and less than 20 g in mass) it is a challenge for the flapping wing vehicle to perform in adverse weather conditions (i.e., wind gust and precipitation). One tactic is to provide adaptability or shape control of the wing structure that can create effective aerodynamic forces (*3*).

Analysis of insect flight indicates that in addition to the bending excitation (flapping), simultaneous excitation of the twisting degree-of-freedom (pitching) is required to manipulate the control surface adequately (*2*). Traditionally, bimorph piezoelectric $Pb(Zr,Ti)O_3$ (also referred to as PZT) actuators have been used in many applications to excite the bending degree-of-freedom. A common bimorph configuration, as shown in figure 1, consists of two thin ceramic plates bonded together and driven with opposing electrical fields. One plate expands while the other contracts, resulting in a bending deflection of the bimorph construction. As a result, a flapping motion is generated from operating at the fundamental resonance frequency of the system (*4*).

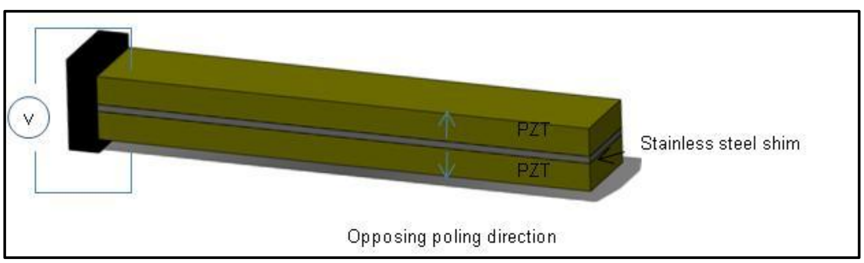

Figure 1. Conventional bimorph actuator.

In prior work, a flapping mechanism was developed that couples a 3 cm PZT-5H bimorph actuator oscillating at resonance frequency with flexural wing joints placed at the distal end of the bimorph (see figure 2). However, in the current approach bend-twist coupling arises from anisotropic material symmetry. In laminated or layered structures, bend-twist coupling is governed by the existence of at least one anisotropic layer not aligned with the primary plate axes (*5*). By adding to a bimorph PZT actuator a layer of off-axis PZT segments active, thereby producing a layered structure to be referred to as a functionally–modified bimorph, bend-twist coupling may be introduced to the flexural response of the layered PZT. Furthermore, by selectively charging off-axis layers in specific combinations with the bimorph, the response of the functionally–modified bimorph may be tailored yielding a biaxial actuator to actively control the flapping wing response.

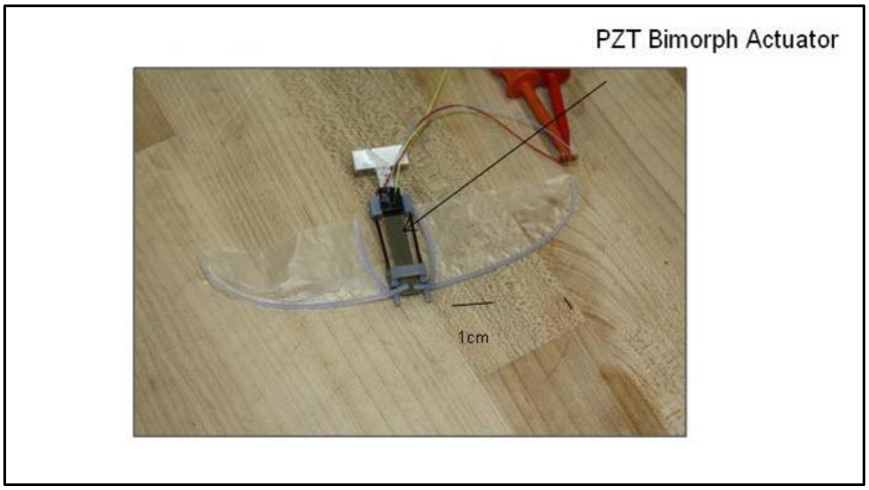

Figure 2. Flapping wing device.

Several studies have considered the use of piezoelectric actuators to drive the bending degree-of-freedom of cantilevered beams for applications ranging from control surfaces of aerospace structures (*6*) to smart rotorcraft blades (*7*, *8*). Piezoelectric cantilevered bimorph actuators for optical deflection and modulation in MEMS applications have been investigated by applying an Euler-Bernoulli beam analysis to clamped bender configurations (*9*). Studies have also been presented that use energy methods (*10*) and elasticity solutions (*11*) to develop quasi-static bending solutions that yielded parametric relationships between tip deflection, applied loads and moments, actuator geometrical dimensions and material properties. The present study develops a numerical solution to the three-dimensional bending analysis of a cantilevered functionally-modified bimorph to investigate the effects of angled segment geometry and orientation on the bimorph bending response.

2. Geometry and Nomenclature

A conventional PZT bimorph cantilever configuration functionalized by the addition of angled PZT segments shown in figure 3 was considered. The coordinate axis referred to as *x*-*y*-*z* is shown in figure 4, where the origin is fixed at the clamped end of the functionalized bimorph at the base of the bottom layer. For the purpose of analysis, the functionally-modified bimorph was idealized as a homogeneous base with homogeneous angle segments attached on top, consisting of transversely isotropic PZT-5H material (Young's modulus, E = 65 GPa). The stainless steel shim depicted in figure 3 was ignored

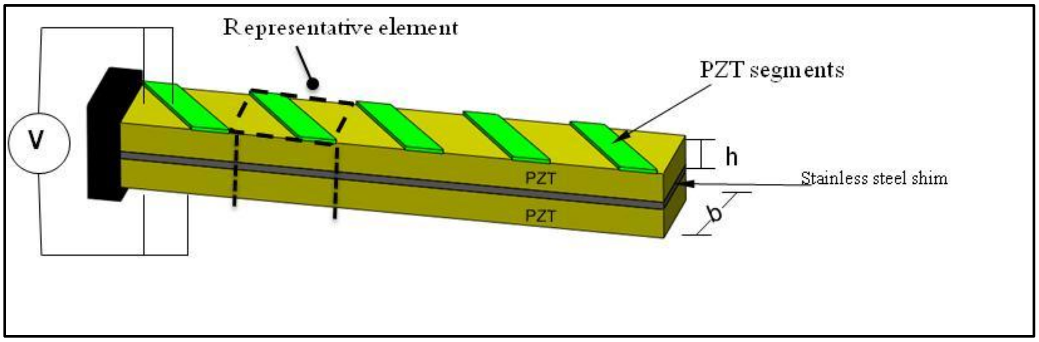

Figure 3. Functionally-modified bimorph.

The distance from the origin to the midplane of the base along the z-axis was h. The total thickness of the base bimorph was $2h$, and the thickness of the angled segments was h. The width b shown in figure 3 relates to the thickness h as follows: $b = 0.1\ h$. The angle of the PZT segments was θ as shown in figure 4. The width of each angled segment measured along the x-axis was d, as shown in figure 5. The overall length L_T of the functionalized bimorph included five angled segments separated by distance s as shown in figure 4.

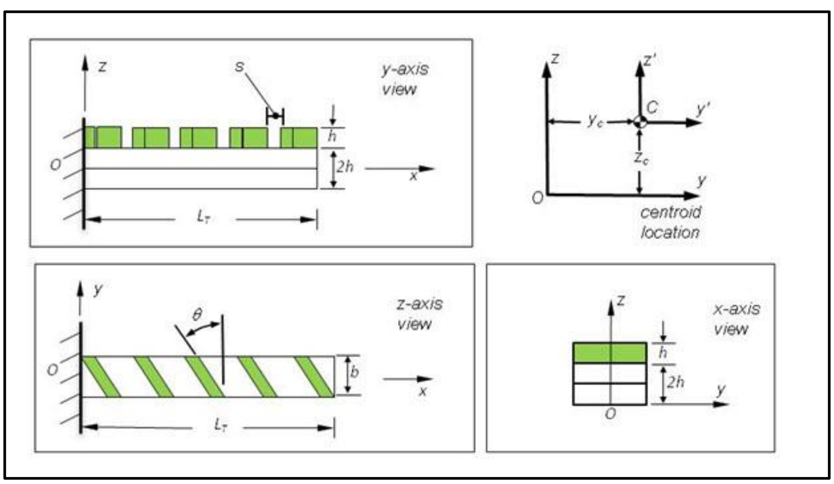

Figure 4. Coordinate system.

In order to develop section properties and geometrical relationships useful for design of PZT configurations, a representative element of the functionalized bimorph was defined to consist of a single angled segment affixed to a bimorph layer shown in figure 5.

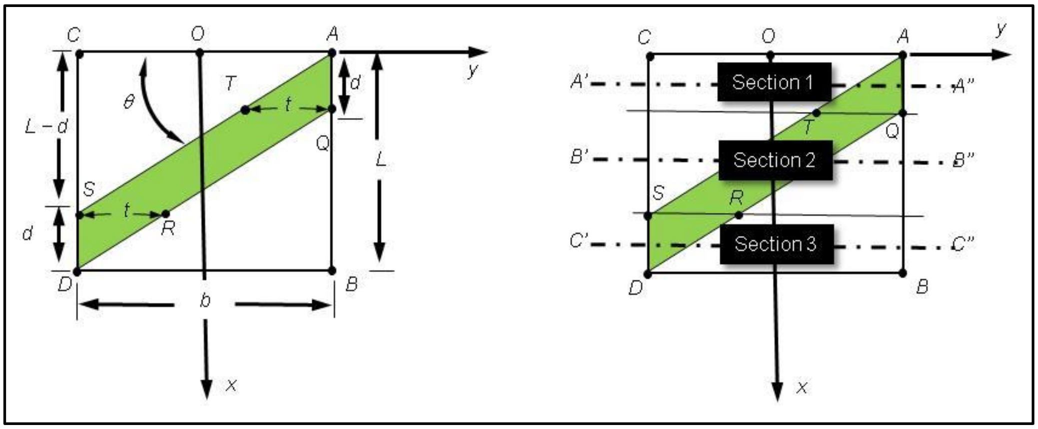

Figure 5. Representative element.

The representative element length, *L*, shown in figure 5, was divided into three distinct regions, namely, sections 1, 2, and 3. Typical cross-sections for are shown in figure 6, where the shaded regions represent the angled segment. Using the described geometry and the points *A*, *B*, *C*, and *D* and points *Q*, *R*, *S*, and *T* shown in figure 5, functional relations for *y*-axis locations along the edges of the angle segments were derived, and are presented below. Section 1 ($0 \leq x < d$), was bounded in *y*-*z* by the plane containing the origin *O* and the points *A* and *C* at $x = 0$ and the plane containing points *Q* and *T* at $x = d$. As *x* increased from 0 to *d*, the width of the angled segment increased from 0 to *t* with respect to the *y*-axis. The section 1 cross-section typified by the *y*-*z* plane at *A′*- *A″* in figure 6 was characterized by the angled segment where the *y*-location of edge *AQ* was fixed at $y = b/2$ and interior edge *AT* was a function of *x*:

$$y_{AT}(x) = \frac{b}{2} - \frac{t}{d}x \quad . \tag{1}$$

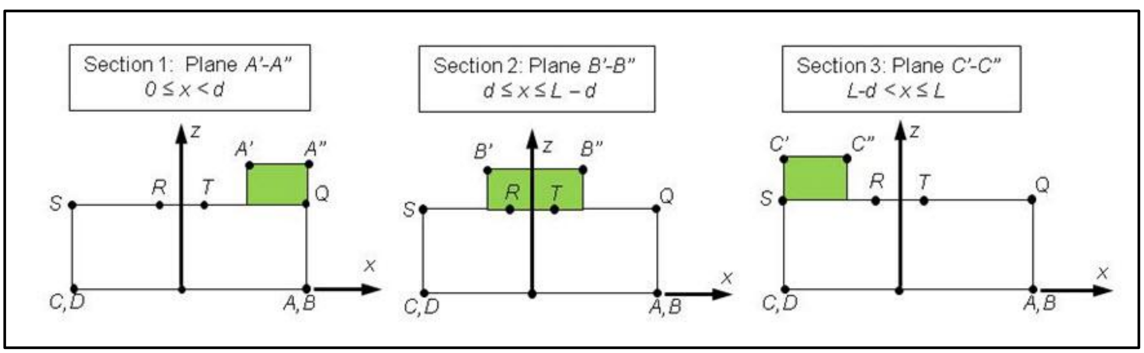

Figure 6. Three representative element typical cross-sections.

Section 2 ($d \le x \le L - d$) was bounded in *y-z* by the plane containing points *Q* and *T* at $x = d$, and at $x = L - d$ by the plane containing points *R* and *S*. As *x* increased from *d* to $L - d$, the width of the angled segment remained constant at *t*. The section 2 cross-section typified by the *y-z* plane *B′-B″* in figure 6 was characterized by the angled segment where the *y*-locations of both edges *QR* and *TS* were functions of *x:*

$$y_{QR}(x) = \frac{t-b}{L-2d}(x-d) + \frac{b}{2} \tag{2}$$

$$y_{TS}(x) = \frac{b-t}{L-2d}(L-d-x) - \frac{b}{2} \tag{3}$$

Section 3 ($L - d < x \le L$) was bounded in *y-z* by the plane containing the points *R* and *S* at $x = L - d$, and the plane containing points *B* and *D* at $x = L$. As *x* increased from $L - d$ to *L*, the width of the angled segment decreased from *t* to 0 with respect to the *y*-axis. The section 3 cross-section typified by the *y-z* plane *C′- C″* in figure 6 was characterized by the angled segment where the *y*-location of interior edge *RD* is a function of *x* and edge *SD* is fixed at $y = -b/2$:

$$y_{RD}(x) = \frac{t}{d}(L-x) - \frac{b}{2}. \tag{4}$$

The following relationships defined axial and transverse width parameters *d* and *t*,

$$d = L - b\tan\theta \tag{5}$$

$$t = \tan\left(\frac{\pi}{2} - \theta\right)d\,. \tag{6}$$

The geometry of the representative element prescribed constraints on the angled segment width parameters *d* and *t*—namely, $d > 0$ and $t < b$. Applying the constraints on the width to the relationships of equations 5 and 6 yielded the following bounds on θ, thus defining angled segment orientation,

$$\cot^{-1}(2b/L) < \theta < \tan^{-1}(L/b)\,. \tag{7}$$

3. Analysis

The results of traditional bending analyses have been used to relate bimorph loading and geometry. For the functionally-modified bimorph considered in the present analysis, the cross-section of the cantilevered bimorph was not symmetric in respect to the horizontal (*x-y*) plane. Therefore, a three-dimensional bending analysis was applied in order to relate the actuator loading and geometric properties to tip deflection (*12*). In order to gain a complete understanding of the complex three-dimensional analysis the piezoelectric effects will be not be considered here.

Beginning with the Euler-Bernoulli assumptions—(1) the cross-section is infinitely rigid in its own plane; (2) the cross-section of a beam remains plane after deformation; and (3) the cross-section remains normal to the deformed axis of the beam—it was assumed that no torsional loads are applied and that the beam bends without twisting. Finally making the assumption that the origin of the coordinate axis system was selected to align with the centroid of the beam as shown in figure 4, the following set of equations govern three-dimensional bending (*12*):

$$\frac{d^2}{dx^2}\left[H^c_{zz}\frac{d^2\bar{v}}{dx^2}+H^c_{yz}\frac{d^2\bar{w}}{dx^2}\right]=p_y+\frac{d}{dx}\left[y_a p_x-q_z\right] \tag{8}$$

$$\frac{d^2}{dx^2}\left[H^c_{yz}\frac{d^2\bar{v}}{dx^2}+H^c_{yy}\frac{d^2\bar{w}}{dx^2}\right]=p_z+\frac{d}{dx}\left[z_a p_x-q_y\right] \tag{9}$$

where, $\bar{v}(x)$ and $\bar{w}(x)$ represented displacements of the beam cross-section in the *y*- and *z*-directions, respectively. Distributed loads along the *x*-axis in the *x*-, *y*-, and *z*-directions were defined as $p_x(x)$, $p_y(x)$, and $p_z(x)$, respectively. Coordinates (y_a, z_a) defined the location in the *y*-*z* plane of the axial distributed load $p_x(x)$. Distributed moments along the *x*-axis about the *y*- and *z*-axes were defined as $q_y(x)$ and $q_z(x)$, respectively. The boundary conditions for the fixed end of the cantilevered bimorph were given by

$$\bar{v}=\bar{w}=0; \quad d\bar{v}/dx=d\bar{w}/dx=0; \tag{10}$$

At the free end, the boundary conditions were as follows (with the shorthand notation in the parentheses) (*12*):

$$\begin{aligned}
&H^c_{zz}\frac{d^2\bar{v}}{dx^2}+H^c_{yz}\frac{d^2\bar{w}}{dx^2}=Q_z-y_aP_x \quad \left(M_z=Q_z-y_aP_x\right)\\
&H^c_{yz}\frac{d^2\bar{v}}{dx^2}+H^c_{yy}\frac{d^2\bar{w}}{dx^2}=-Q_y-z_aP_x \quad \left(M_y=Q_y-z_aP_x\right)\\
&-\frac{d}{dx}\left[H^c_{zz}\frac{d^2\bar{v}}{dx^2}+H^c_{yz}\frac{d^2\bar{w}}{dx^2}\right]=P_y-\left[y_ap_x-q_z\right] \quad \left(V_y=P_y\right)\\
&-\frac{d}{dx}\left[H^c_{yz}\frac{d^2\bar{v}}{dx^2}+H^c_{yy}\frac{d^2\bar{w}}{dx^2}\right]=P_z-\left[z_ap_x+q_y\right] \quad \left(V_z=P_z\right)
\end{aligned} \tag{11}$$

where P_y and P_z represented applied shear at the tip in the respective *y*- and *z*-directions. Applied bending moments in the *y*- and *z*-directions were represented by Q_y and Q_z, respectively. In the shorthand notation (equation 11 in parentheses), *M* and *V* represented the internal moments and shears, respectively. The centroidal bending stiffness coefficients H_{yy}, H_{zz}, and H_{yz} were defined

$$H_{yy} = H_{yy}^c + Sz_c^2; \quad H_{zz} = H_{zz}^c + Sy_c^2; \quad H_{yz} = H_{yz}^c + Sy_c z_c; \tag{12}$$

where, H_{yy}, H_{zz}, and H_{yz} represent the bending stiffness coefficients with respect to an arbitrary coordinate axis:

$$H_{yy} = \int_A Ez^2 dA; \quad H_{zz} = \int_A Ey^2 dA; \quad H_{yz} = \int_A EyzdA; \tag{13}$$

where, E was the Young's modulus and y and z refer to coordinates of an arbitrary point in the y-z plane. Note here that the bending stiffness coefficients are functions of beam cross-sectional area in the y-z plane. For the functionally-modified bimorph, as the bimorph geometry traverses the x-axis, the beam cross-section in y-z is dependent on the relationships for y as a function of x developed in equations 1–4. Therefore, the coefficients of the ordinary differential governing equations of equations 8 and 9 and the boundary conditions in equation 11 are functions of x, and are considered to be variable coefficients. Generally, ordinary differential equations with variable coefficients must be solved numerically.

The sectional stiffness coefficients S, S_y, and S_z are defined as follows (note that the coefficient S_y is a function of x):

$$S = \int_A EdA; \quad S_y = \int_A EydA; \quad S_z = \int_A EzdA; \tag{14}$$

the centroid of a the beam cross-section (y_c,z_c) as shown in figure 4 is defined in terms of section stiffness coefficients

$$y_c = \frac{S_y}{S} \quad z_c = \frac{S_z}{S}. \tag{15}$$

Again, note that the centroidal location y_c varies with x-location along the beam. In order to perform the three-dimensional bending analysis of the functionally-modified bimorph, the beam was considered in sections along its length (x-axis) by defining a representative element, as shown in figure 5. The governing equations applied to the sections of the representative element shown in figure 5, take on the following piece-wise form:

$$\begin{aligned} 0 \le x < d: \quad & \frac{d^2}{dx^2}\left[H_{zz}^c \frac{d^2\overline{v}_1}{dx^2} + H_{yz}^c \frac{d^2\overline{w}_1}{dx^2}\right] = 0 \\ & \frac{d^2}{dx^2}\left[H_{yz}^c \frac{d^2\overline{v}_1}{dx^2} + H_{yy}^c \frac{d^2\overline{w}_1}{dx^2}\right] = 0 \end{aligned} \tag{16}$$

$$\begin{aligned} d \le x < L - d: \quad & \frac{d^2}{dx^2}\left[H_{zz}^c \frac{d^2\overline{v}_2}{dx^2} + H_{yz}^c \frac{d^2\overline{w}_2}{dx^2}\right] = 0 \\ & \frac{d^2}{dx^2}\left[H_{yz}^c \frac{d^2\overline{v}_2}{dx^2} + H_{yy}^c \frac{d^2\overline{w}_2}{dx^2}\right] = 0 \end{aligned} \tag{17}$$

$$L-d \le x \le L: \quad \frac{d^2}{dx^2}\left[H^c_{zz}\frac{d^2\overline{v}_3}{dx^2}+H^c_{yz}\frac{d^2\overline{w}_3}{dx^2}\right]=0$$
$$\frac{d^2}{dx^2}\left[H^c_{yz}\frac{d^2\overline{v}_3}{dx^2}+H^c_{yy}\frac{d^2\overline{w}_3}{dx^2}\right]=0 \tag{18}$$

where, the subscripts on $\bar{v}(x)$ and $\overline{w}(x)$ represent the sections of the representative element as depicted in figure 5. The boundary conditions for a concentrated load *P* applied to the free end of the cantilevered bimorph configuration assumed, using the shorthand notation from equation 11

$$\begin{aligned} x=0: &\quad \overline{v}_1=\overline{w}_1=0; \quad d\overline{v}_1/dx=d\overline{w}_1/dx=0; \\ x=L_T: &\quad M_{y_3}=0 \\ &\quad M_{z_3}=0 \\ &\quad V_{y_3}=0 \\ &\quad V_{z_3}=-P \end{aligned} \tag{19}$$

Additionally, the following continuity conditions were applied to allow the analysis to span the sections of the piece-wise representative element, where the displacements and slopes at the junctions of the segments were defined as being equal:

$$\begin{aligned} x=d: &\quad \overline{v}_1=\overline{v}_2; \quad \overline{w}_1=\overline{w}_2; \quad d\overline{v}_1/dx=d\overline{v}_2/dx; \quad d\overline{w}_1/dx=d\overline{w}_2/dx; \\ x=L-d: &\quad \overline{v}_2=\overline{v}_3; \quad \overline{w}_2=\overline{w}_3; \quad d\overline{v}_2/dx=d\overline{v}_3/dx; \quad d\overline{w}_2/dx=d\overline{w}_3/dx. \end{aligned} \tag{20}$$

In order, to find the deflection of the entire functionally-modified bimorph, continuity conditions were applied to a series of representative elements with spaces of traditional bimorph in-between as shown in figure 4. The result of this process was a system of 38 fourth order coupled variable coefficient ordinary differential equations (ODEs). The system of ODEs was solved numerically using the built-in symbol **NDSolve** in *Mathematica** Version 8 (*13*) to find the tip displacement in terms of bimorph geometrical parameters. Results for the deflection of the cantilevered functionally-modified bimorph in respect to angled segment geometry and orientation are presented in the next section.

4. Results and Discussion

The angled segments of the functionally-modified bimorph formed an angle θ with the clamped edge of the bimorph as shown in the inset in figure 7. Equations 5 and 6 provided the relationships between the angle θ and geometric parameters that govern length *L*, angled segment widths *b* and *t*. Figure 7 shows the upper and lower bounds on θ as defined by equations 5 and 6, respectively. The points labeled in figure 7 as I–VII correspond to the case numbers in table 1.

* *Mathematica* is a trademark of Wolfram Research, Inc.

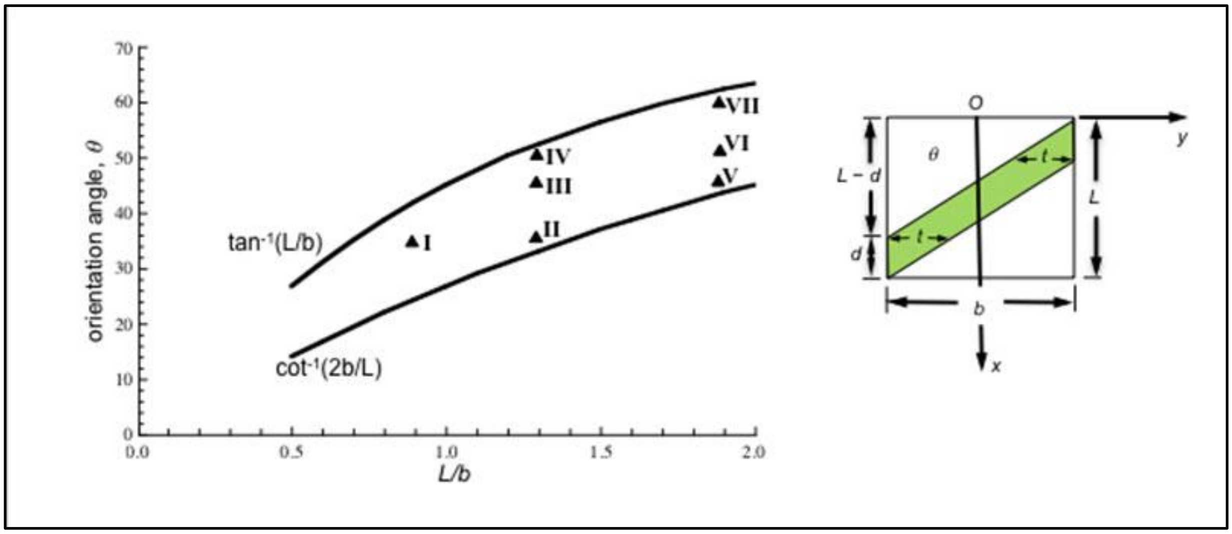

Figure 7. Upper and lower bounds on angled segment orientation angle θ.

Presented in table 1 are three-dimensional bending results for the bimorph configuration of figure 4, where b was fixed at 6 mm and exposed to an applied tip shear P = 1.0 N in the negative z (downward) direction. Cases I and II (labeled in figure 6) shared the same θ orientation for different ratios of length L and width b. Because b was fixed, decreasing L/b ratio indicated increasing L; therefore, the length of the representative element in Case II was greater. The maximum section displacement results occurred at the $x = L_T$ tip location. The results for Cases I and II predicted that maximum deflection increases as length L increases, indicating a strong dependence on overall length L_T.

Table 1. Representative element results for b = 6 mm exposed to P = 1.0 N concentrated load in negative z-direction (downward).

Case	**L/b**	**θ**	**d/L**	v_{max} **(10^{-6} m)**	w_{max} **(10^{-3} m)**
I	0.9	34°	0.35	–0.355	–0.0572
II	1.3	34°	0.48	–0.161	–0.121
III	1.3	45°	0.23	–0.134	–0.148
IV	1.3	51°	0.050	–0.997	–0.134
V	1.9	45°	0.47	–0.643	–0.374
VI	1.9	51°	0.35	–2.239	–0.331
VII	1.9	60°	0.085	–2.667	–0.322

Comparison of Cases III and V of table 1, also labeled in figure 7, further evidenced the dependence of the maximum deflection value on bimorph length. Cases III and V shared the same value of θ. The length of the Case V configuration was greater than Case III. The maximum deflection increased as length increased. Also, considering Cases IV and VI, where θ values were similar between the two cases. The length of Case VI was greater, and maximum deflection for Case VI was greater. The results in table 1 clearly establish that there is a strong dependence of maximum deflection on overall bimorph length. Namely, as length increases, maximum deflection increases.

Figure 8 presents the deflection curves for Cases II, III, and IV, where the θ values are given by 34°, 45°, and 51° respectively. Each case, as shown in table 1, had a L/b ratio of 1.3, implying an overall length L_T = 28 mm. Here, as θ increased, d/L decreased, indicating a decrease in the width of the angled segment. Intuitively, the increase in θ would seem to imply an increase in the stiffening capability of the segment. However, as shown in figure 8, Case III at θ = 45°, d/L = 0.23, displayed the greatest deflection and was therefore the least stiff configuration, while for Cases II and IV, both configurations displayed greater stiffness, compared with Case III, as segment width increased and decreased, respectively.

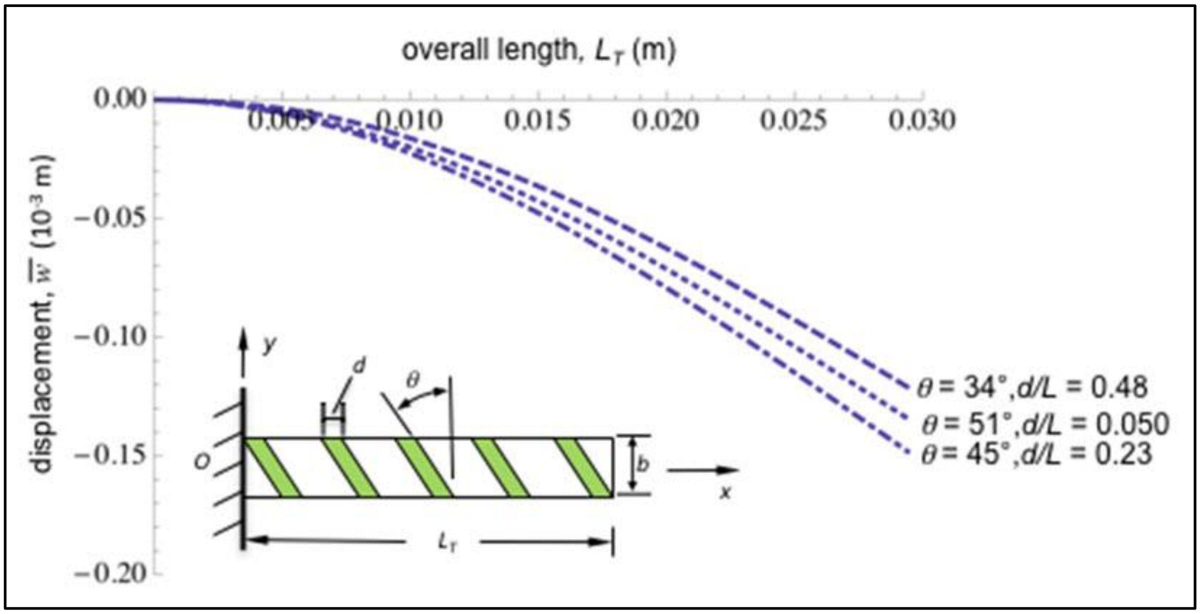

Figure 8. Deflection results for Cases II, III, and IV.

Figure 9 shows the relationship of deflection and angled segment orientation θ for L/b = 1.3. The data showed that as θ increased between the bounds prescribed by the representative element geometry, the deflection reached a maximum at around θ = 45° and decreased until it reached the upper bound on θ. As θ increased, the data in figure 9 show that the width parameter d/L indicated decreasing width d. The change in the width of the angled segment resulted in a change in the section bending stiffness coefficients H_{yy}, H_{zz}, and H_{yz} defined in equation 12. As θ increased to θ = 45°, the section bending stiffness coefficients decreased to a value that nearly coincided with the section properties for the traditional bimorph (without the angled segments). Therefore, due to the change in angled segment width brought about by the change in angle θ, the section properties influenced the bending response so that the resistance to bending in the bimorph decreased. Thus, the orientation and width of the angled segments interacted in such a way that the bending capacity of the traditional bimorph served as a lower bound on deflection.

The increase in deflection after $\theta = 45°$ may have been due to error typical to numerical solutions.

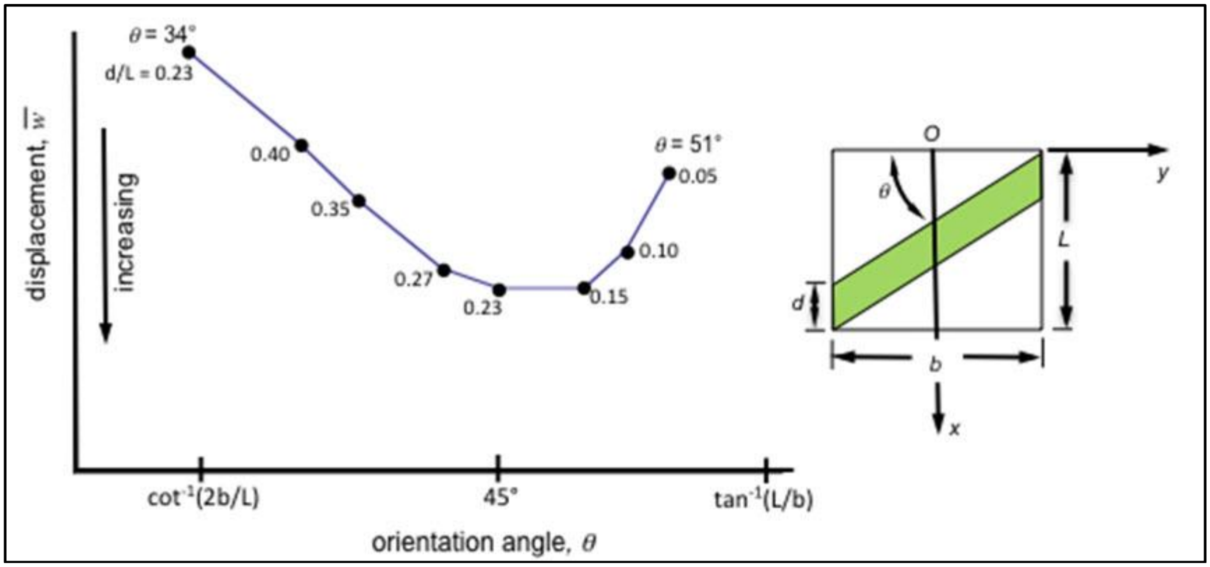

Figure 9. Effect of orientation angle θ on functionally-modified bimorph deflection for L/b = 1.3.

---

5. Conclusions

A quasi-static three-dimensional bending analysis of a functionally-modified bimorph configuration has been presented. The analysis was conducted on an idealized configuration where angled PZT segments were assumed to be affixed to a base traditional bimorph configuration. The presence of the metal shim was neglected analytically. In general, bimorph deflection increased with increase in bimorph length. For fixed bimorph length L_T, as θ increases, deflection increases, due to changes in the bimorph sectional stiffness properties. The prescribed geometry of the functionally-modified bimorph configuration provided constraints on the orientation angle of the PZT segments affixed to the bimorph surface. The orientation and width of the angled segments interacted in such a way that the bending properties of the traditional bimorph act as a lower bound on deflection. Future work will include numerical validation of the three-dimensional bending analysis via finite-element analysis and experimental validation, with the ultimate goal of developing a design tool for biaxial actuators for *cm*-scale flapping wing MAVs.

6. References

1. Mueller, T. J. *Fixed and Flapping Wing for Micro Air Vehicles*, AIAA Inc.: Reston, VA, 2001, pp 1–10.

2. Wu, P.; Ifju, P. Flapping Wing Effectiveness, Efficiency and Aeroelasticity Relationships. *48th AIAA Aerospace Sciences Meeting*, Orlando, FL, January 4–7, 2010, (*1017*), pp 1–15.

3. Lewitowicz, J.; Kowalczyk, G.; Sibilski, K.; Zurek, J. Modeling and Simulation of Flapping Wings Micro-aerial-vehicles Flight Dynamics. *26th International Congress of the Aeronautical Sciences (ICAS)*, Anchorage, AK, September 14–19, 2008; pp 1–24.

4. Hall, A.; Pekala, M. C. Micro-electro Mechanical Flapping Wing Technology for Micro Air Vehicles. *IMAV 2010 Proceedings*, Braunschweig, Germany, July 6–9, 2010; pp 1–6.

5. Wetherhold, R. C.; Aldraheim, O. J. Bending and Twisting Vibration Control of Flexible Structures Using Piezoelectric Materials. *Shock and Vib. Dig.* **2001**, *33* (3), 187–197.

6. Crawley, E. F.; de Luis, J. Use of Piezoelectric Actuators as Elements of Intelligent Structures. *AIAA J.* **1987**, *25* (10) 1373–1385.

7. Aldraheim, O. J.; Wetherhold, R. C. Mechanics and Control of Coupled Bending and Twisting Vibration of Laminated Beams. *Smart Mtls. and Struct.* **1997**, *6*, 123–133.

8. Park, C.; Walz, C.; Chopra, I. Bending and Torsion Models of Beams with Induced-Strain Actuators. *Smart Mtls. and Struct.* **1996**, *5*, 98–113.

9. Ballato, A.; Kim, Y. Displacements and Rotations of Practical Vibrational Modes of Piezoelectric Bimorph Cantilever Beams. *Proceedings of First IEEE International Conference on Sensors*, Orlando, FL, June 12–14, 2002, 2, pp 1294–1297.

10. Smits, J. G.; Dalke, S. I.; Cooney, T. K. The Constituent Equations of Piezoelectric Bimorphs. *Sens. and Act. A* **1991**, *28*, 41–61.

11. Wang, Q.-M.; Cross, L. E. Performance Analysis of Piezoelectric Cantilever Bending Actuators. Ferroelec. **1998**, *215* (1), 187–213.

12. Bauchau, O. A.; Craig, J. I. *Structural Analysis: With Applications to Aerospace Structures*; Springer: Dordrecht, Heidelberg, London & New York, 2009, pp 171–202.

13. Wolfram, S. *The Mathematica Book*; Wolfram Media/Cambridge University Press: Champaign, Cambridge, New York, and Melbourne, 1999.

NO. OF COPIES	ORGANIZATION
1 (PDF only)	DEFENSE TECHNICAL INFORMATION CTR DTIC OCA 8725 JOHN J KINGMAN RD STE 0944 FORT BELVOIR VA 22060-6218
1	DIRECTOR US ARMY RESEARCH LAB IMNE ALC HRR 2800 POWDER MILL RD ADELPHI MD 20783-1197
1	DIRECTOR US ARMY RESEARCH LAB RDRL CIO LL 2800 POWDER MILL RD ADELPHI MD 20783-1197
1	DIRECTOR US ARMY RESEARCH LAB RDRL CIO MT 2800 POWDER MILL RD ADELPHI MD 20783-1197
1	DIRECTOR US ARMY RESEARCH LAB RDRL D 2800 POWDER MILL RD ADELPHI MD 20783-1197
	ABERDEEN PROVING GROUND
3	US ARMY RESEARCH LAB ATTN RDRL VTM J RIDDICK A HALL M BUNDY APG MD 21005

INTENTIONALLY LEFT BLANK.